Comput. Methods Appl. Mech. Engrg. 199 (2010) 780–790

Contents lists available at ScienceDirect

Comput. Methods Appl. Mech. Engrg.

journal homepage: www.elsevier.com/locate/cma

Isogeometric variational multiscale modeling of wall-bounded turbulent flows with weakly enforced boundary conditions on unstretched meshes

Y. Bazilevs [a,*], C. Michler [b], V.M. Calo [b], T.J.R. Hughes [b]

[a] Department of Structural Engineering, University of California, San Diego, 9500 Gilman Drive MC0085, La Jolla, CA 92093, USA
[b] Institute for Computational Engineering and Sciences, The University of Texas at Austin, 201 East 24th Street, 1 University Station C0200, Austin, TX 78712, USA

ARTICLE INFO

Article history:
Received 25 April 2008
Received in revised form 29 August 2008
Accepted 5 November 2008
Available online 13 December 2008

Keywords:
Incompressible flow
Navier–Stokes equations
Boundary layers
Turbulence
Law of the wall
Weakly imposed boundary conditions
Isogeometric Analysis
Preconditioning
Turbulent channel flow
Planar asymmetric diffuser flow

ABSTRACT

In this work, we combine (i) NURBS-based isogeometric analysis, (ii) residual-driven turbulence modeling and iii) weak imposition of no-slip and no-penetration Dirichlet boundary conditions on unstretched meshes to compute wall-bounded turbulent flows. While the first two ingredients were shown to be successful for turbulence computations at medium-to-high Reynolds number [I. Akkerman, Y. Bazilevs, V. M. Calo, T. J. R. Hughes, S. Hulshoff, The role of continuity in residual-based variational multiscale modeling of turbulence, Comput. Mech. 41 (2008) 371–378; Y. Bazilevs, V.M. Calo, J.A. Cottrell, T.J.R. Hughes, A. Reali, G. Scovazzi, Variational multiscale residual-based turbulence modeling for large eddy simulation of incompressible flows, Comput. Methods Appl. Mech. Engrg., 197 (2007) 173–201], it is the weak imposition of no-slip boundary conditions on coarse uniform meshes that maintains the good performance of the proposed methodology at higher Reynolds number [Y. Bazilevs, T.J.R. Hughes. Weak imposition of Dirichlet boundary conditions in fluid mechanics, Comput. Fluids 36 (2007) 12–26; Y. Bazilevs, C. Michler, V.M. Calo, T.J.R. Hughes, Weak Dirichlet boundary conditions for wall-bounded turbulent flows. Comput. Methods Appl. Mech. Engrg. 196 (2007) 4853–4862]. These three ingredients form a basis of a possible practical strategy for computing engineering flows, somewhere between RANS and LES in complexity. We demonstrate this by solving two challenging incompressible turbulent benchmark problems: channel flow at friction-velocity Reynolds number 2003 and flow in a planar asymmetric diffuser. We observe good agreement between our calculations of mean flow quantities and both reference computations and experimental data. This lends some credence to the proposed approach, which we believe may become a viable engineering tool.

1. Introduction

An LES-type variational multiscale theory of turbulence was recently proposed in [5]. The methodology derives completely from the Navier–Stokes equations and does not resort to ad hoc filtering and eddy viscosities. Unlike earlier variational multiscale approaches, wherein filtering was replaced by the variational projection and eddy viscosity was confined to the explicitly represented small scales [25–27,40,31,19,29,33,16,42,17], in this recent work all scales were viewed as resolved scales and no eddy viscosity was introduced in the method. An important conclusion of [5] is that the success of numerical formulations for turbulent flows depends to a large degree on the quality of the approximation spaces employed in the computations. A dispersion analysis using simple model problems was performed in [5], which showed that NURBS elements are superior to classical finite elements in approximating advective and diffusive processes, which play a significant role in turbulence computations. In turbulent channel flow problems quadratic NURBS gave very significant accuracy improvements over linear finite elements. Moreover, it was demonstrated in [1] that the continuity of the basis functions plays a critical role in turbulence calculations, especially for flows at higher Reynolds number.

Although the numerical results in [5] were very good and confirmed the viability of the newly proposed technique for LES computations, suboptimal results were obtained in the presence of unresolved turbulent boundary layers. To rectify this situation, Bazilevs and Hughes [7] and Bazilevs et al. [8] proposed to satisfy wall Dirichlet boundary conditions weakly rather than strongly. Weak imposition of no-slip boundary conditions entails augmenting the variational multiscale formulation of the Navier–Stokes equations by terms that enforce the Dirichlet conditions weakly as Euler-Lagrange conditions at the no-slip wall. This has led to significantly improved results for the computation of turbulent channel flows at medium-to-high Reynolds numbers; see [8].

In [7,8], we imposed the no-slip boundary condition pertaining to the tangential velocity components weakly, while the no-penetration condition pertaining to the wall-normal velocity component was imposed strongly. Such strong imposition entails the construction of a discrete normal vector at mesh nodes. This

* Corresponding author.
E-mail address: yuri@ucsd.edu (Y. Bazilevs).

0045-7825/$ - see front matter © 2008 Elsevier B.V. All rights reserved.
doi:10.1016/j.cma.2008.11.020

normal vector is used to enforce the discrete no-penetration condition. The latter is implemented in the left-hand-side matrix and right-hand-side vector by rotations from the global Cartesian coordinate system to local coordinate systems defined by a normal and two tangential vectors (see, e.g., Gresho and Sani [18] for details). In the present work, we modify the original weak Dirichlet condition formulation by imposing also the no-penetration boundary condition weakly. Since it is well-known that the normal velocity does not experience large gradients in the turbulent boundary layer, we do not expect a great improvement in accuracy by releasing the normal component. However, imposing all components of the velocity boundary conditions weakly considerably simplifies computer implementation and allows for a unified treatment of Dirichlet boundary conditions. Furthermore, additional computational effort is insignificant.

In this work, we make use of NURBS-based isogeometric analysis [23,14,6,4,53] in combination with variational multiscale, residual-driven turbulence modeling and weak enforcement of wall boundary conditions to solve two challenging turbulence benchmark test cases: turbulent channel flow at friction-velocity based Reynolds number of $Re_\tau = 2003$ and turbulent flow in an asymmetric diffuser. The former test case is the highest Reynolds number channel flow for which there exists high-fidelity DNS data [20], while the latter has only recently emerged as a turbulence benchmark for which experimental results [41,10] as well as computational results at the level of LES resolution [32,52,17] are available.

The paper is organized as follows. In Section 2, we present the weak formulation of the continuous problem for the incompressible Navier–Stokes equations. We then state the discrete, residual-based variational multiscale formulation of the problem with no-slip Dirichlet boundary conditions imposed weakly. In Section 3, we describe the numerical procedures that we use to solve the nonlinear equations focusing on the solution of the systems of linear equations that arise in the linearization of the flow equations. In particular we describe the *assembled element-by-element inverse preconditioner* that we developed and routinely use in our computations. In Section 4, we show numerical results for an equilibrium turbulent channel flow at $Re_\tau = 2003$. In Section 5, we present results for the turbulent asymmetric diffuser problem. In Section 6, we draw conclusions.

2. Weak imposition of Dirichlet boundary conditions for the incompressible Navier–Stokes equations

2.1. Continuous problem

We begin by considering a weak formulation of the incompressible Navier–Stokes equations. We will describe the simple case of zero velocity boundary condition. Other boundary conditions will be treated later in the context of particular problems. Let $\mathscr{V}$ denote the trial and weighting function spaces, which are assumed to be the same.

The variational formulation is stated as follows: Find a velocity–pressure pair, $\boldsymbol{U} = \{\boldsymbol{u}, p\} \in \mathscr{V}$, such that for all weighting functions $\boldsymbol{W} = \{\boldsymbol{w}, q\} \in \mathscr{V}$

$$B(\boldsymbol{W}, \boldsymbol{U}) = F(\boldsymbol{W}), \tag{1}$$

where

$$B(\boldsymbol{W}, \boldsymbol{U}) = \left(\boldsymbol{w}, \frac{\partial \boldsymbol{u}}{\partial t}\right)_\Omega - (\nabla \boldsymbol{w}, \boldsymbol{u} \otimes \boldsymbol{u})_\Omega + (q, \nabla \cdot \boldsymbol{u})_\Omega - (\nabla \cdot \boldsymbol{w}, p)_\Omega + (\nabla^s \boldsymbol{w}, 2\nu \nabla^s \boldsymbol{u})_\Omega, \tag{2}$$

and

$$F(\boldsymbol{W}) = (\boldsymbol{w}, \boldsymbol{f})_\Omega. \tag{3}$$

in which ν is the kinematic viscosity, p is the pressure divided by the fluid density, and $\boldsymbol{f}$ is the body force. Under suitable smoothness hypotheses, (1)–(3) imply strong forms of linear momentum balance and incompressibility, namely

$$\mathscr{L}(\boldsymbol{u}, p) - \boldsymbol{f} = \boldsymbol{0} \text{ in } \Omega, \tag{4}$$

$$\nabla \cdot \boldsymbol{u} = 0 \quad \text{in } \Omega, \tag{5}$$

where

$$\mathscr{L}(\boldsymbol{u}, p) = \frac{\partial \boldsymbol{u}}{\partial t} + \nabla \cdot (\boldsymbol{u} \otimes \boldsymbol{u}) + \nabla p - \nabla \cdot (2\nu \nabla^s \boldsymbol{u}). \tag{6}$$

In the sequel we also utilize the advective form of (4) obtained by employing (5):

$$\mathscr{L}_{\text{adv}}(\boldsymbol{u}, p) = \frac{\partial \boldsymbol{u}}{\partial t} + \boldsymbol{u} \cdot \nabla \boldsymbol{u} + \nabla p - \nu \Delta \boldsymbol{u}. \tag{7}$$

2.2. Discrete formulation

Find $\boldsymbol{U}^h = \{\boldsymbol{u}^h, p^h\} \in \mathscr{V}^h \subset \mathscr{V}$ such that $\forall \boldsymbol{W}^h = \{\boldsymbol{w}^h, q^h\} \in \mathscr{V}^h \subset \mathscr{V}$,

$$B_{\text{MSW}}(\boldsymbol{W}^h, \boldsymbol{U}^h) - F_{\text{MSW}}(\boldsymbol{W}^h) = 0, \tag{8}$$

where

$$\begin{aligned} B_{\text{MSW}}(\boldsymbol{W}^h, \boldsymbol{U}^h) &= B_{\text{MS}}(\boldsymbol{W}^h, \boldsymbol{U}^h) \\ &+ \sum_{b=1}^{n_{eb}} (\boldsymbol{w}^h, (\boldsymbol{u}^h \cdot \boldsymbol{n})\boldsymbol{u}^h + p^h \boldsymbol{n} - 2\nu \nabla^s \boldsymbol{u}^h \cdot \boldsymbol{n})_{\Gamma_b \cap \Gamma} \\ &+ \sum_{b=1}^{n_{eb}} (-2\nu \nabla^s \boldsymbol{w}^h \cdot \boldsymbol{n} - q^h \boldsymbol{n}, \boldsymbol{u}^h - \boldsymbol{0})_{\Gamma_b \cap \Gamma_{out}} \\ &+ \sum_{b=1}^{n_{eb}} (-2\nu \nabla^s \boldsymbol{w}^h \cdot \boldsymbol{n} - q^h \boldsymbol{n} - (\boldsymbol{u}^h \cdot \boldsymbol{n})\boldsymbol{w}^h, \boldsymbol{u}^h - \boldsymbol{0})_{\Gamma_b \cap \Gamma_{in}} \\ &+ \sum_{b=1}^{n_{eb}} (\boldsymbol{w}^h \tau_B, \boldsymbol{u}^h - \boldsymbol{0})_{\Gamma_b \cap \Gamma} \\ &+ \sum_{b=1}^{n_{eb}} \left(\boldsymbol{w}^h \cdot \boldsymbol{n}\left(\frac{C_b^I \nu}{h_b} - \tau_B\right), \boldsymbol{u}^h \cdot \boldsymbol{n} - 0\right)_{\Gamma_b \cap \Gamma}, \end{aligned} \tag{9}$$

$$\begin{aligned} B_{\text{MS}}(\boldsymbol{W}^h, \boldsymbol{U}^h) &= B(\boldsymbol{W}^h, \boldsymbol{U}^h) \\ &+ \sum_{e=1}^{n_{el}} ((\boldsymbol{u}^h \cdot \nabla \boldsymbol{w}^h + \nabla q^h)\tau_M, \mathscr{L}_{\text{adv}}(\boldsymbol{u}^h, p^h) - \boldsymbol{f})_{\Omega_e} \\ &+ \sum_{e=1}^{n_{el}} ((\boldsymbol{u}^h \cdot (\nabla \boldsymbol{w}^h)^T)\tau_M, \mathscr{L}_{\text{adv}}(\boldsymbol{u}^h, p^h) - \boldsymbol{f})_{\Omega_e} \\ &- \sum_{e=1}^{n_{el}} (\nabla \boldsymbol{w}^h, \tau_M(\mathscr{L}_{\text{adv}}(\boldsymbol{u}^h, p^h) - \boldsymbol{f}) \otimes \tau_M(\mathscr{L}_{\text{adv}}(\boldsymbol{u}^h, p^h) - \boldsymbol{f}))_{\Omega_e} \\ &+ \sum_{e=1}^{n_{el}} (\nabla \cdot \boldsymbol{w}^h, \tau_C \nabla \cdot \boldsymbol{u}^h)_{\Omega_e}, \end{aligned} \tag{10}$$

and

$$F_{\text{MSW}}(\boldsymbol{W}^h) = (\boldsymbol{w}^h, \boldsymbol{f})_\Omega, \tag{11}$$

where $\Omega = \bigcup_{e=1}^{n_{el}} \Omega_e$, Ω_e is an element domain and n_{el} is the number of elements, and Γ_{in} and Γ_{out} are the inflow ($\boldsymbol{u}^h \cdot \boldsymbol{n} < 0$) and outflow ($\boldsymbol{u}^h \cdot \boldsymbol{n} \geqslant 0$) parts of the Dirichlet boundary, respectively. In order to understand why certain terms in (10) are ostensibly omitted, see [5], Section 4. The subscripts MS and MSW stand for "multiscale" and "multiscale weak", respectively.

In Eqs. (8)–(11) we employ the following definitions

$$\tau_M := \left(\frac{C_t}{\Delta t^2} + \boldsymbol{u}^h \cdot \boldsymbol{G}\boldsymbol{u}^h + C_I \nu^2 \boldsymbol{G} : \boldsymbol{G}\right)^{-1/2}, \tag{12}$$

$$\tau_C := (\boldsymbol{g} \cdot \tau_M \boldsymbol{g})^{-1}, \tag{13}$$

$$\boldsymbol{G} = \left(\frac{\partial \boldsymbol{\xi}}{\partial \boldsymbol{x}}\right)^T \frac{\partial \boldsymbol{\xi}}{\partial \boldsymbol{x}}, \tag{14}$$

$$\boldsymbol{g} = (\boldsymbol{g})_i = \sum_{j=1}^{d} \left(\frac{\partial \boldsymbol{\xi}}{\partial \boldsymbol{x}}\right)_{ji}, \tag{15}$$

$$h_b = 2(\boldsymbol{n}^T \boldsymbol{G} \boldsymbol{n})^{-1/2}. \tag{16}$$

$\frac{\partial \xi}{\partial \boldsymbol{x}}$ is the inverse Jacobian of the element mapping between the parent and the physical domain, $\boldsymbol{n}$ is a unit outward normal vector to the fluid domain boundary, and C_I^b, C_t and C_I are positive constants. Note that for rectangular meshes Eq. (16) gives the element length in the wall-normal direction. τ_B in (9) is defined as

$$\tau_B := \frac{u^{*2}}{||\boldsymbol{u}^h_{\tan}||}, \tag{17}$$

where u^* is the so-called wall-friction velocity that satisfies the following non-linear algebraic equations

$$y^+ = f(u^+) = u^+ + e^{-\chi B}\left(e^{\chi u^+} - 1 - \chi u^+ - \frac{(\chi u^+)^2}{2} - \frac{(\chi u^+)^3}{6}\right), \tag{18a}$$

$$y^+ := \frac{y u^*}{\nu}, \tag{18b}$$

$$u^+ := \frac{||\boldsymbol{u}^h_{\tan}||}{u^*}. \tag{18c}$$

In Eqs. (18a)–(18c), y^+ and u^+ denote the non-dimensional distance from the wall and mean fluid speed, respectively, $y = h_b/C_I^b, \boldsymbol{u}^h_{\tan}$ is the tangential velocity vector, and $\chi = 0.4$ and $B = 5.5$. Eq. (18a) is Spalding's parameterization of a turbulent boundary layer [48] that is valid over the entire range of y^+, from the viscous sublayer to the end of the logarithmic layer. For a detailed development of weak boundary conditions based on the wall function formulation see [8].

Remarks.

(1) The above formulation is a residual-based variational multiscale method for the incompressible Navier–Stokes equations (see e.g. [11,22,3,5]) that is based on the variational multiscale (VMS) methodology; see, e.g., [28]. Parameters τ_M and τ_C are designed by asymptotic scaling developed within the theory of stabilized methods (see, e.g., [9,24,45,50]).

(2) The last five terms of (9) pertain to the weak enforcement of the no-slip condition, as presented in [7], inspired by the Symmetric Interior Penalty Galerkin Discontinuous Galerkin method [51]. The fifth-to-last term in (9) is the so-called consistency term: When deriving the Euler-Lagrange equations corresponding to (9), integration-by-parts yields a term that is canceled by the consistency term. The fourth-to-last and third-to-last terms in (9) are the so-called adjoint-consistency terms: If the exact solution of the adjoint problem is inserted into Eq. (9) in place of the test function, (9) is satisfied identically; see [2] for details on adjoint consistency. The last two terms of (9) penalize the deviation of the discrete solution from the Dirichlet boundary condition.

(3) The constants C_t, C_I and C_I^b are independent of the mesh size and are selected to ensure the stability and optimal rate of convergence of the method (see [13,7] for details).

(4) As a result of imposing the no-penetration condition weakly, additional terms arise in the method as compared to the original formulation in [8]. Advective and pressure parts of the traction operator are now present in the consistency term. The test function of the continuity equation, q^h, appears in the weighting of the Dirichlet terms. As a result, the Dirichlet condition pertaining to the wall-normal direction is weighted more heavily than the Dirichlet conditions in the remaining directions. Note that the terms involving pressure and the continuity test function enter into the formulation in a skew-symmetric fashion, which is stability neutral. Moreover, the treatment of the inflow and outflow parts of the Dirichlet boundary differs. In accordance with [7], on Γ_{in}, we also include the advective part of the traction operator acting on $\boldsymbol{w}^h$ in the weighting terms for the Dirichlet boundary condition. We use different penalty parameters for enforcing the tangential and normal components of the Dirichlet conditions. A wall-function based penalty is used for the tangential component, while a purely numerical penalty is used for the normal component, because the law of the wall is assumed to hold only for the tangential velocity components.

3. The assembled element-by-element inverse preconditioner

In this section, we describe the element-by-element inverse preconditioner that is used in the solution of the linear systems arising from linearization of the incompressible flow equations.

In the sequel, A is the nodal index in standard finite element analysis, and the control point index in NURBS-based isogeometric analysis, $\boldsymbol{e}_i$ is the i^{th} Cartesian basis vector and $\boldsymbol{V}$ and $\boldsymbol{P}$ denote the vectors of control-variable degrees-of-freedom of velocity and pressure, respectively. We assume that velocity and pressure are expanded in terms of the same basis, denoted by $\{N_A\}_{A=1}^{n_b}$, where n_b is the number of basis functions. We define two residual vectors corresponding to the momentum and continuity equations by substituting in (8) $N_A\boldsymbol{e}_i$ and N_A for $\boldsymbol{w}^h$ and q^h, respectively, which yields

$$\boldsymbol{R}^M = [R^M_{A,i}], \tag{19}$$

$$R^M_{A,i} = B_{MSW}(\{N_A\boldsymbol{e}_i, 0\}, \{\boldsymbol{u}^h, p^h\}) - F_{MSW}(\{N_A\boldsymbol{e}_i, 0\}), \tag{20}$$

$$\boldsymbol{R}^C = [R^C_A], \tag{21}$$

$$R^C_A = B_{MSW}(\{\boldsymbol{0}, N_A\}, \{\boldsymbol{u}^h, p^h\}) - F_{MSW}(\{\boldsymbol{0}, N_A\}). \tag{22}$$

We employ the generalized-α method to advance Eqs. (19)–(22) in time. This leads to a nonlinear system of equations to be solved at each time step for which we employ a Newton–Raphson procedure. During each Newton step we solve the linear system

$$\begin{bmatrix} \partial \boldsymbol{R}^M/\partial \boldsymbol{V} & \partial \boldsymbol{R}^M/\partial \boldsymbol{P} \\ \partial \boldsymbol{R}^C/\partial \boldsymbol{V} & \partial \boldsymbol{R}^C/\partial \boldsymbol{P} \end{bmatrix} \begin{Bmatrix} \Delta \boldsymbol{V} \\ \Delta \boldsymbol{P} \end{Bmatrix} = \begin{Bmatrix} -\boldsymbol{R}^M \\ -\boldsymbol{R}^C \end{Bmatrix}, \tag{23}$$

where $\Delta\boldsymbol{V}$ and $\Delta\boldsymbol{P}$ denote the solution increments of velocity and pressure. For the details of the time integration and linearization see [5]. Here, we focus on the technique that we use to solve the linear system (23).

To fix ideas, consider the simple case in which there is only one degree-of-freedom per node or control point. This might correspond to a problem involving the scalar advection–diffusion equation, for example. (The case of the Navier–Stokes equations involves multiple degrees-of-freedom per node or control point, but the concepts are similar.) Let $\mathop{\mathbf{A}}_{e=1}^{n_e}$ denote the standard finite-element assembly operator (see, e.g., Hughes [21]) that maps a collection of element-level matrices $\boldsymbol{k}^e$'s onto a global matrix $\boldsymbol{K}$ (typically stored in sparse format) as

$$\boldsymbol{K} = \mathop{\mathbf{A}}_{e=1}^{n_e} \boldsymbol{k}^e, \tag{24}$$

$$\boldsymbol{K} = [K_{IJ}], \tag{25}$$

$$\boldsymbol{k}^e = [k^e_{ij}], \tag{26}$$

where I and J are the global basis function indices, i and j are the local (element-level) basis function indices, and n_e is the number of elements in the mesh. The mapping (24) may algorithmically be expressed as

$$\begin{aligned} &\boldsymbol{K} = \boldsymbol{0} \\ &\text{for } e = 1, n_e \\ &\quad \text{for } i = 1, n_l \\ &\quad\quad \text{for } j = 1, n_l \\ &\quad\quad\quad K_{IEN(i,e),IEN(j,e)} = K_{IEN(i,e),IEN(j,e)} + k^e_{i,j} \\ &\quad\quad \text{end} \\ &\quad \text{end} \\ &\text{end} \end{aligned} \tag{27}$$

In (27), $IEN(i,e)$ assigns a global basis function number to a local basis function number i in every element of the mesh e, and is therefore commonly known as the connectivity array. n_l is the number of local basis functions for every element. The above algorithm extends straightforwardly to the multiple degree-of-freedom case.

For subsequent use we also define the *extraction operator* $\mathop{\mathbf{E}}_{e=1}^{n_e}$, which, in contrast to the assembly operator $\mathop{\mathbf{A}}_{e=1}^{n_e}$, maps a global matrix onto a collection of local matrices as

$$\hat{\boldsymbol{k}}^e = \mathop{\mathbf{E}}_{e=1}^{n_e} \boldsymbol{K} \tag{28}$$

$\mathop{\mathbf{E}}_{e=1}^{n_e}$ extracts element-level matrices from the global matrix and may algorithmically be expressed as

$$\begin{aligned}
&\text{for } e = 1, n_e \\
&\quad \text{for } i = 1, n_l \\
&\quad\quad \text{for } j = 1, n_l \\
&\quad\quad\quad \hat{k}^e_{i,j} = K_{IEN(i,e),IEN(j,e)} \\
&\quad\quad \text{end} \\
&\quad \text{end} \\
&\text{end}
\end{aligned} \tag{29}$$

Note that, given a collection of element-level matrices, applying first the assembly operator and then the extraction operator does not return the original local matrices. This is due to the fact that typically more than one local basis function is assigned to one global basis function.

To specify the preconditioner, we define the matrix $\boldsymbol{A}$

$$\boldsymbol{A} = \begin{bmatrix} \partial \boldsymbol{R}^M / \partial \boldsymbol{V} & \partial \boldsymbol{R}^M / \partial \boldsymbol{P} \\ \partial \boldsymbol{R}^C / \partial \boldsymbol{V} & \partial \boldsymbol{R}^C / \partial \boldsymbol{P} \end{bmatrix}, \tag{30}$$

the right-hand-side vector $\boldsymbol{b}$

$$\boldsymbol{b} = \begin{Bmatrix} -\boldsymbol{R}^M \\ -\boldsymbol{R}^C \end{Bmatrix}, \tag{31}$$

the solution vector $\boldsymbol{x}$

$$\boldsymbol{x} = \begin{Bmatrix} \Delta \boldsymbol{V} \\ \Delta \boldsymbol{P} \end{Bmatrix}, \tag{32}$$

and rewrite (23) as

$$\boldsymbol{A}\boldsymbol{x} = \boldsymbol{b}. \tag{33}$$

Our preconditioner, denoted by $\tilde{\boldsymbol{A}}$, is constructed by first extracting element-level matrices $\boldsymbol{a}^e$ from $\boldsymbol{A}$ as

$$\boldsymbol{a}^e = \mathop{\mathbf{E}}_{e=1}^{n_e} \boldsymbol{A}, \tag{34}$$

then inverting the element-level matrices[1]

$$\tilde{\boldsymbol{a}}^e = (\boldsymbol{a}^e)^{-1}, \tag{35}$$

and finally assembling the $\tilde{\boldsymbol{a}}^e$'s into the inverse of the preconditioner $\widetilde{\boldsymbol{A}}^{-1}$ as

$$\widetilde{\boldsymbol{A}}^{-1} = \mathop{\mathbf{A}}_{e=1}^{n_e} \tilde{\boldsymbol{a}}^e. \tag{36}$$

Then, left-preconditioning the system (33) yields

$$\widetilde{\boldsymbol{A}}^{-1}\boldsymbol{A}\boldsymbol{x} = \widetilde{\boldsymbol{A}}^{-1}\boldsymbol{b}, \tag{37}$$

which we solve using the GMRES algorithm (see Saad and Schultz [44]) to a specified tolerance.

[1] We compute the inverse of the element matrices using the routines from the LAPACK library [37].

Remarks.

(1) The above preconditioner makes use of structures specific to finite elements and is thus suitable for finite-element calculations. It is based on element-by-element strategies (see, e.g., [15]).
(2) We choose to extract the element-level matrices from the global matrix rather than use the element-level matrices that are computed "on the fly" in the routines that assemble the global matrix for the following reasons: (*i*) this procedure removes possible singularities from the element matrices that may arise due to, for instance, rigid body modes; (*ii*) coupling with the neighboring elements is introduced; (*iii*) this procedure may be implemented at the level of a linear solver, which typically makes use of assembled matrices.
(3) The preconditioner matrix $\widetilde{\boldsymbol{A}}$ has the same sparsity structure as A and, thus, no additional data structures need to be implemented.
(4) This preconditioner may be understood as an additive Schwarz procedure (see, e.g., [43] pp. 472–473) where the restriction operator restricts the global matrix to its element-level counterpart.

4. Turbulent channel flow at $Re_\tau = 2003$

We conduct numerical experiments for turbulent channel flow at Reynolds numbers $Re_\tau = 2003$, with Re_τ based on the friction velocity and the channel half width. To assess the accuracy of our methodology, we compare our results to the DNS results of [20].

4.1. Problem setup

The flow is driven by a pressure gradient in the stream-wise direction. At the computational domain boundary, periodic boundary conditions are imposed in both stream-wise and span-wise directions, whereas a homogeneous Dirichlet boundary condition is applied in the wall-normal direction.

For the spatial discretization we employ NURBS-based isogeometric analysis [23]. For the rectangular geometry considered in this example, NURBS reduce to simple B-splines. We use quadratic NURBS basis functions that are C^1-continuous at knots. This is in contrast to standard quadratic finite-element functions that are only C^0-continuous across element boundaries. Recent studies have shown the NURBS discretization to be superior to standard finite elements on a per-degree-of-freedom basis for phenomena involving convection and diffusion such as turbulent flow; see [1,5]. We also would like to point out that B-spline functions have been successfully used for turbulence computations previously in [34,46,35,36].

We employ meshes of 64^3 and 128^3 elements that are uniform in all directions. For the mesh with 64^3 elements the first knot lies at $y^+ \approx 62$, whereas for the mesh with 128^3 elements the first knot lies at $y^+ \approx 31$. Thus, in either case, we intentionally sacrifice the resolution of the boundary layer.

The domain size is 6π, 2, and 2π in the stream-wise, wall-normal and span-wise directions, respectively. The corresponding DNS used a domain size of $8\pi \times 2 \times 3\pi$ with a resolution of $6144 \times 633 \times 4608$ functions in the stream-wise, wall-normal and span-wise directions. Details of the computational setup are given in Table 1.

The semi-discrete equations are advanced in time using the generalized-α method with $\rho_\infty = 0.5$, where ρ_∞ is the spectral radius of the amplification matrix as $\Delta t \to \infty$, which controls high-frequency dissipation; see [21,12,30]. In all cases we use a time

Table 1
Details of the computational setup of the $Re_\tau = 2003$ channel. $L_{x,y,z}$ denotes the length of the channel in the stream-wise, wall-normal and span-wise direction, respectively, N_{el} is the number of elements in the domain, $N_{x,y,z}$ is the number of basis functions in the stream-wise, wall-normal and span-wise direction, respectively, f_x is the forcing in the stream-wise direction, and ν denotes kinematic viscosity. Due to the open knot vector construction (see [23] for details), the number of basis functions in the wall-normal direction exceeds the corresponding number of elements by the polynomial order p (here, $p = 2$).

	L_x	L_y	L_z	N_{el}	N_x	N_y	N_z	f_x	ν
Coarse	6π	2	2π	64^3	64	66	64	$2.125985 \cdot 10^{-3}$	$2.3020 \cdot 10^{-5}$
Fine	6π	2	2π	128^3	128	130	128	$2.125985 \cdot 10^{-3}$	$2.3020 \cdot 10^{-5}$

step of 0.025 based on the mean stream-wise flow velocity of unity. Moreover, we set $C_t = 4, C_I = 36$ and $C_b^I = 4$.

Linear equations were solved to a relative tolerance of 10^{-3} in terms of the l^2 norm of the left-preconditined residual. For the 64^3 case the minimum number of GMRES iterations was set to 20, while for the 128^3 case this number was increased to 30. For both cases, for each time step in the first Newton iteration, convergence to a tolerance was achieved before the minimum number of GMRES iterations was reached. During the third (and last) Newton iteration convergence to the prescribed tolerance was reached in approximately 40 and 75 GMRES iterations for the 64^3 and 128^3 cases, respectively.

As initial condition we use a randomly perturbed Poiseuille flow profile, where the fluctuations do no exceed 15% of the mean stream-wise velocity magnitude. We perform time-integration until a statistically stationary, fully developed turbulent flow is reached. Further time-integration is carried out to collect statistics of the flow. Defining as a "flow-through" the time that it takes for a fluid particle to traverse the length of the channel, we collect data over ten flow-throughs, sampling on average 3.5 times per flow-through. Numerical results for all cases are reported in the form of statistics of the mean velocity and root-mean-square of the velocity fluctuations. Statistics are computed by sampling the velocity field at the mesh knots and averaging the solution in time as well as in the stream-wise and span-wise directions. Results are presented in non-dimensional wall units.

4.2. Numerical results

As mentioned previously, we use two uniform meshes of different resolution. A 64^3 mesh that allows a relatively inexpensive comparison between the method given in Eqs. (8)–(11) with the method proposed in Ref. [8], and a 128^3 mesh to assess the performance of the method given in Eqs. (8)–(11) under h-refinement. We investigate two ways of applying homogeneous Dirichlet boundary conditions at the wall: First, we impose both tangential and normal velocity components weakly according to Eqs. (8)–(11). Second, we impose only the tangential velocity components weakly and enforce the wall-normal component strongly as in Ref. [8]. Figs. 1,2 show primary and secondary statistics of the computations on the two meshes considered.

Fig. 1 demonstrates that the difference in accuracy between the "all weak" formulation given in Eqs. (8)–(11) and the "weak tangential" formulation from Ref. [8] is only minor. In particular, on such a coarse mesh, both methods are unable to capture the DNS result accurately, although they do capture the qualitative trend of the features. This suggests that the advantage of the "all weak" formulation over the "weak tangential" formulation merely pertains to implementational convenience rather than to superior accuracy.

Fig. 2 considers only the "all weak" formulation and reveals that a substantial improvement in accuracy can be obtained on a 128^3 mesh in comparison with a 64^3 mesh. In particular, the mean

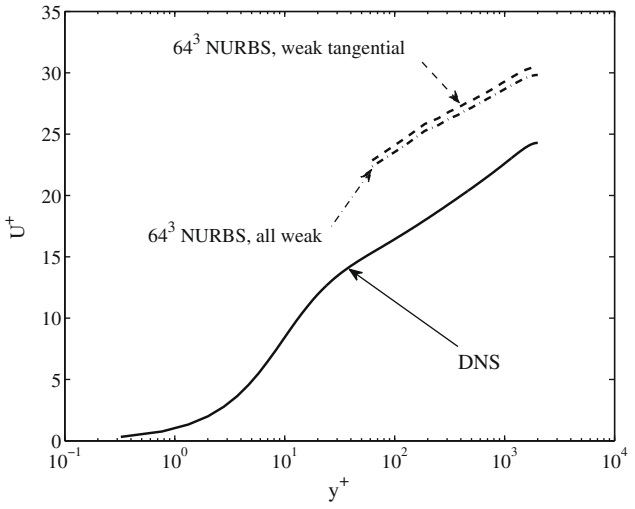

(a) Mean stream-wise velocity

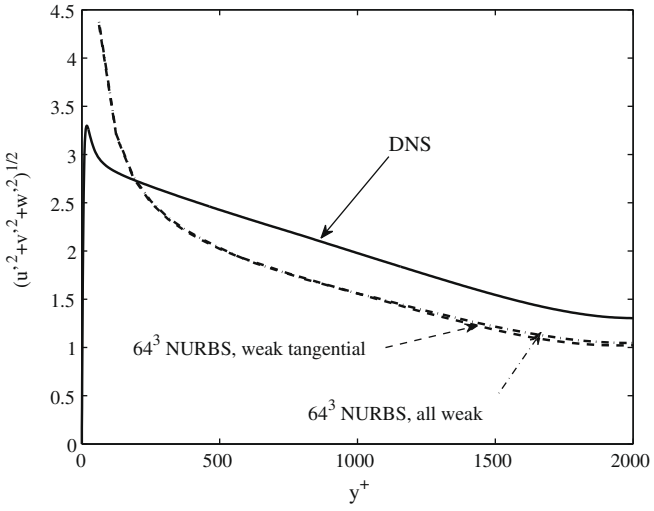

(b) RMS of the velocity fluctuations

Fig. 1. Turbulent channel flow at $Re_\tau = 2003$: Results obtained on uniform 64^3 meshes with the "all weak" formulation given in Eqs. (8)–(11) (- - -) and the "weak tangential" formulation from Ref. [8] (-·-), and comparison with the DNS from Ref. [20] (—).

velocity computed on the 128^3 mesh comes much closer to the DNS result than for the 64^3 case. The accuracy of the velocity fluctuations improves significantly in the region $y^+ < 500$, but hardly at all in the region $y^+ > 500$.

5. Turbulent flow through an asymmetric diffuser

In this section, we present the results for the asymmetric diffuser problem, which has only recently emerged as a numerical benchmark for turbulent flow. The asymmetric planar diffuser problem was investigated experimentally by Obi et al. [41] and Buice and Eaton [10], and numerically by Kaltenbach et al. [32], Wu et al. [52] and Gravemeier [17]. Besides the basic turbulent features, such as highly fluctuating velocities and the presence of thin boundary layers, this test case involves a variety of complex fluid mechanical phenomena. The latter include the presence of a strong adverse pressure gradient, regions of flow separation and reattachment and a slowly growing internal layer; see [52]. The complex nature of the problem and the availability of experimental results as well as reference computations make this test case very attrac-

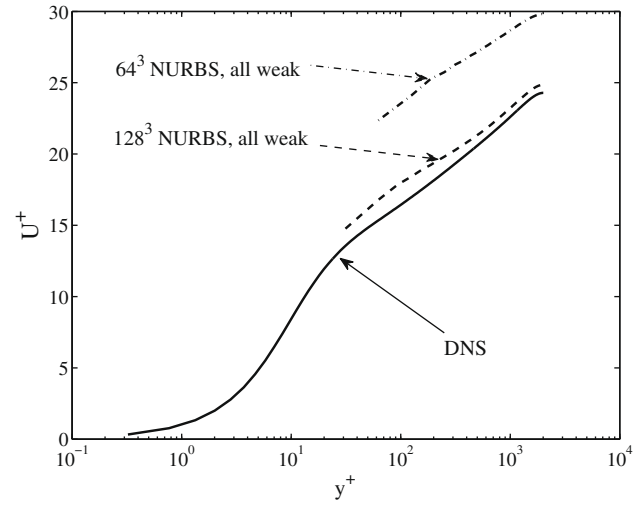

(a) Mean stream-wise velocity

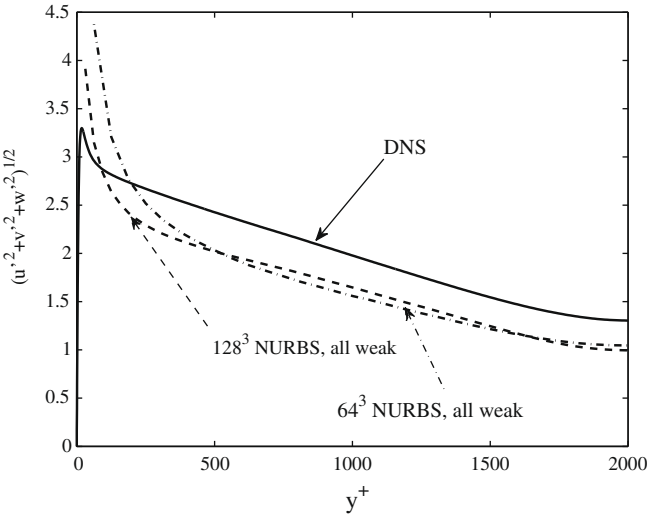

(b) RMS of the velocity fluctuations

Fig. 2. Turbulent channel flow at $Re_\tau = 2003$: Results obtained with the "all weak" formulation given in Eqs. (8)–(11) on a uniform 128^3 mesh (- - -) and a uniform 64^3 mesh (-·-), and comparison with the DNS from Ref. [20] (—).

tive for verification and validation of newly emerging LES turbulence modeling techniques.

The problem setup is illustrated in Fig. 3. The diffuser geometry matches the experimental setup of [41]. The computational setup, including geometry, material data, and forcing, is that of [52,17]. No-slip and no-penetration boundary conditions are applied weakly at the top and bottom walls of the diffuser. In the span-wise direction, periodic boundary conditions are employed to mimic infinite domain size in this direction. At the diffuser outlet the following outflow boundary condition is employed

$$-p\boldsymbol{n} + 2\nu\nabla^s\boldsymbol{u}\cdot\boldsymbol{n} - (\{\boldsymbol{u}\cdot\boldsymbol{n}\}_-)\boldsymbol{u} = \boldsymbol{0} \text{ on } \Gamma_{out}, \tag{38}$$

where the term $\{\boldsymbol{u}\cdot\boldsymbol{n}\}_-$ denotes the negative part of $\boldsymbol{u}\cdot\boldsymbol{n}$, that is

$$\begin{cases} \{\boldsymbol{u}\cdot\boldsymbol{n}\}_- = \boldsymbol{u}\cdot\boldsymbol{n} & \text{if} \quad \boldsymbol{u}\cdot\boldsymbol{n} < 0 \\ \{\boldsymbol{u}\cdot\boldsymbol{n}\}_- = 0 & \text{otherwise} \end{cases}. \tag{39}$$

In the case of reverse flow through Γ_{out}, the last term on the left-hand-side in (38) is active. Otherwise, it is identically zero and, thus, Eq. (38) reverts to the well-known zero-traction or "do-nothing" boundary condition. Imposition of (38) entails adding the following outflow boundary integral term to variational formulation (9)

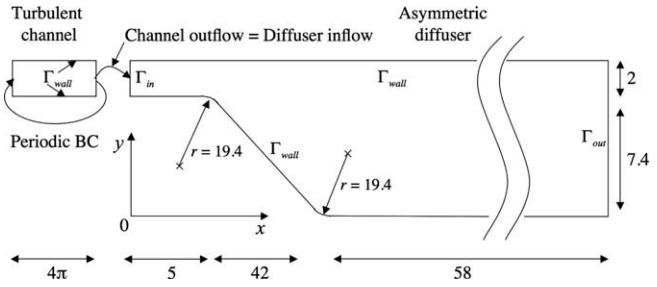

Fig. 3. Setup of asymmetric diffuser problem, planar view. The span-wise dimension of the turbulent channel and the diffuser is chosen to be 8, as in [52,17].

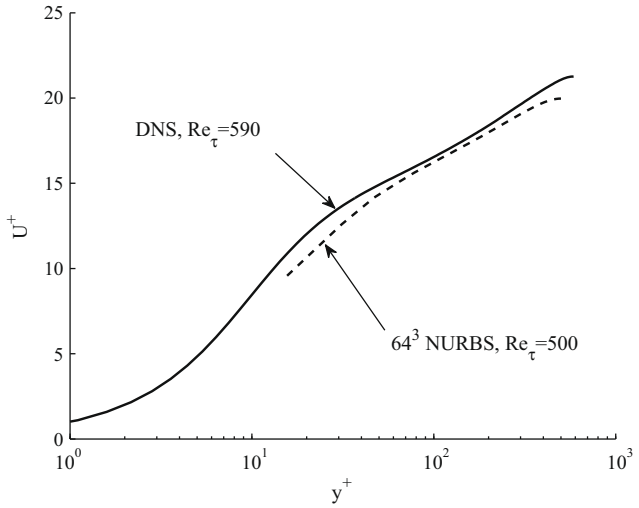

(a) Mean stream-wise velocity

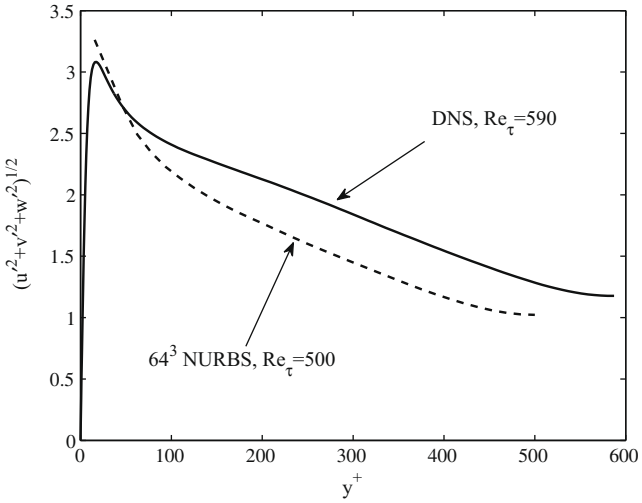

(b) RMS of the velocity fluctuations

Fig. 4. Turbulent channel flow at $Re_\tau = 500$. Note, however, that the DNS data corresponds to $Re_\tau = 590$.

$$+\int_{\Gamma_{out}} \boldsymbol{w}(\{\boldsymbol{u}\cdot\boldsymbol{n}\}_+)\boldsymbol{u}\,d\Gamma_{out}, \tag{40}$$

where the term $\{\boldsymbol{u}\cdot\boldsymbol{n}\}_+$ denotes the positive part of $\boldsymbol{u}\cdot\boldsymbol{n}$, that is

$$\begin{cases} \{\boldsymbol{u}\cdot\boldsymbol{n}\}_+ = \boldsymbol{u}\cdot\boldsymbol{n} & \text{if} \quad \boldsymbol{u}\cdot\boldsymbol{n} > 0 \\ \{\boldsymbol{u}\cdot\boldsymbol{n}\}_+ = 0 & \text{otherwise} \end{cases}. \tag{41}$$

Remark.

(1) The above modification (40) is appropriate if the governing variational equations make use of the conservative form of the convective term, as is done in this work (see Eq. (1)). If the so-called advective form of the convective term is used (see, e.g., Ref. [1]), then the following modification to the governing equations should be introduced

$$-\int_{\Gamma_{out}} \boldsymbol{w}(\{\boldsymbol{u}\cdot\boldsymbol{n}\}_{-})\boldsymbol{u}d\Gamma_{out}. \tag{42}$$

(2) The terms specified in Eqs. (40) and (42) add stability to the formulation in the presence of reverse flow through the outflow boundary. Such reverse flow may, and actually does, occur due to the fact that turbulent structures are being convected out of the computational domain by the mean flow in the stream-wise direction. We found that the addition of term (40) is critical, as in its absence we experience rapid divergence in our computations.

(3) The generalized-α method parameter ρ_∞, the time step, and constants C_t, C_I and C_b^I are the same as for the channel (see Section 4.1).

(4) Linear equations were solved to a relative tolerance of 10^{-3} as for the channel in Section 4.1. The minimum number of GMRES iterations was set to 30. In the first Newton iteration, convergence was achieved before the minimum number of GMRES iterations was reached. During the third Newton iteration convergence was reached in approximately 100 GMRES iterations. We feel that the performance of the assembled element-by-element inverse preconditioner is

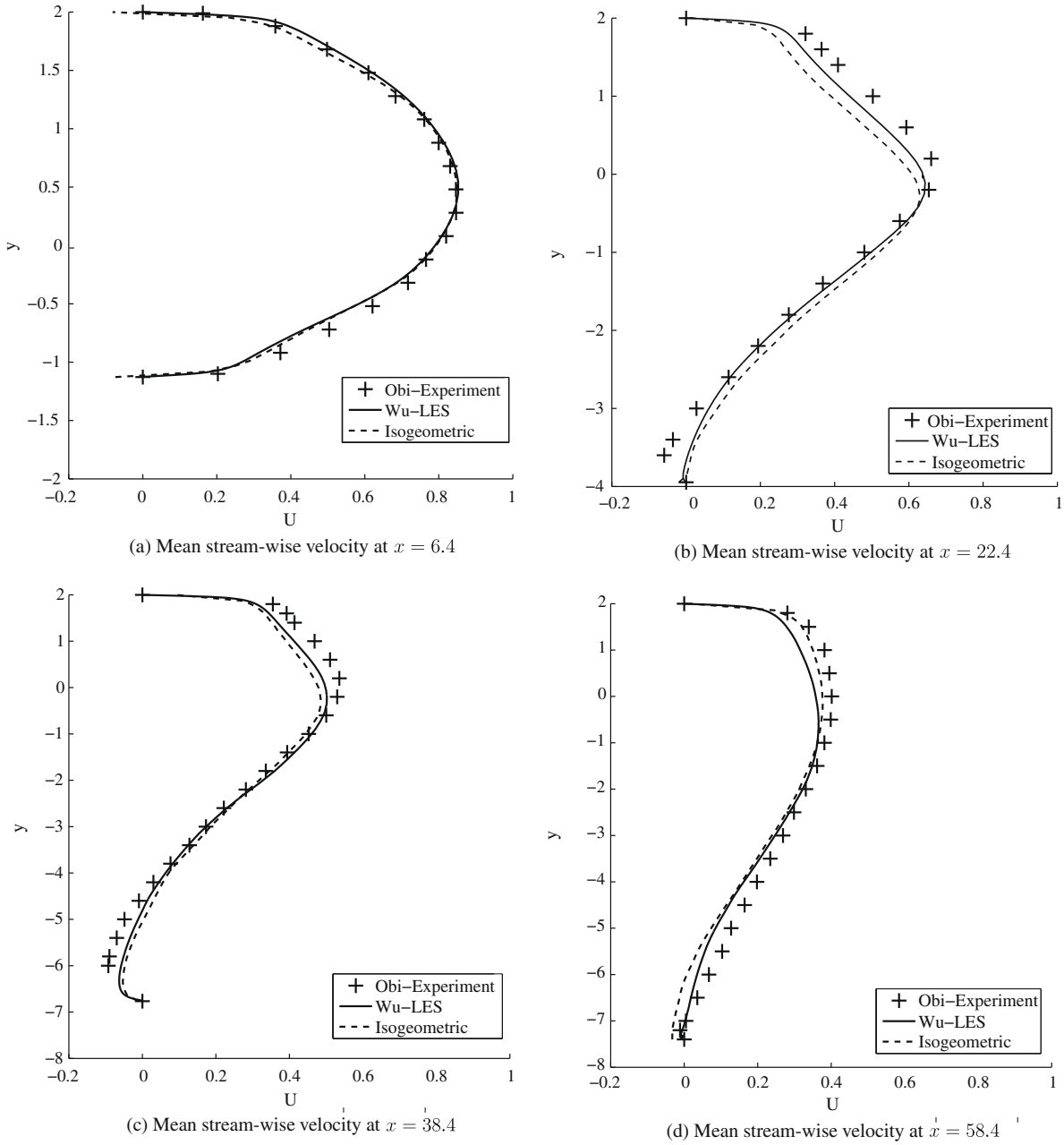

(a) Mean stream-wise velocity at $x = 6.4$

(b) Mean stream-wise velocity at $x = 22.4$

(c) Mean stream-wise velocity at $x = 38.4$

(d) Mean stream-wise velocity at $x = 58.4$

Fig. 5. Flow in an asymmetric diffuser. Statistics of the mean stream-wise velocity.

satisfactory, considering the fact that the domain of the problem is significantly longer in the stream-wise direction than in other directions. For a discussion of difficulties arising in iterative methods for incompressible flows on long domains see, e.g., [38]. Our experience with diagonal preconditioning on long domain problems is that it is effective during the first Newton iteration but it tends to stagnate in the third Newton iteration. On the other hand, the assembled element-by-element inverse preconditioner has behaved robustly in these situations.

The flow in the diffuser is driven by a prescribed inlet velocity boundary condition. The inflow velocity profile is obtained from a separate computation of turbulent channel flow at $Re_\tau = 500$. The channel outflow velocity profile is collected at every time step and imposed strongly as a Dirichlet boundary condition at the diffuser inlet, denoted by Γ_{in} in Fig. 3. For the turbulent channel, the forcing in the stream-wise direction is chosen to be $f_x = 3.160554 \cdot 10^{-3}$ and the kinematic viscosity is $\nu = 1.12438 \cdot 10^{-4}$. With this choice of forcing and viscosity the mean stream-wise velocity at the turbulent channel outlet and, accordingly, at the diffuser inlet, is expected to be approximately 1. The turbulent channel problem is discretized into 64^3 quadratic NURBS elements that are C^1-continuous. The elements are uniform in all tensor-product directions, including the wall-normal direction.

Fig. 4(a) shows the mean flow statistics while Fig. 4(b) depicts the RMS of the velocity fluctuations as a function of the wall-normal distance. Since no DNS data is available for this Reynolds number, we compare our result to the closest available DNS result, viz. the DNS at $Re_\tau = 590$ of Moser, Kim and Mansour [39]. The mean velocity profile expressed in wall units is independent of the Reynolds number considered and, thus, both curves should coincide. The agreement between our result and the DNS is very good in the logarithmic layer, but some deviation is observed in the buffer layer. In contrast to the mean velocity and independent of the scaling employed, the RMS of the sum of velocity fluctuations curves of our computation and the reference are not expected to match. In fact, our RMS of the sum of velocity fluctuations curve lies below the DNS which physically makes sense, as the energy content in the flow at lower Reynolds number is lower. Accuracy of the turbulent channel computation directly translates into accuracy of the inflow boundary condition for the diffuser.

The diffuser makes use of the same kinematic viscosity as the $Re_\tau = 500$ channel and is discretized into $302 \times 64 \times 64$ quadratic NURBS elements that are C^1-continuous. In the stream-wise direction the mesh design follows closely that of Gravemeier [17]. In the vertical direction, to test the weak imposition of boundary conditions, we employ a uniform mesh rather than a stretched mesh that is tailored to an increased resolution in the boundary layer. Due to periodic boundary conditions in the span-wise direction, we use a uniform mesh in this direction as well. Note that, in the beginning and end of the asymmetric section of the diffuser, circular fillets, which are a part of the geometric model (see Fig. 3), are represented exactly in our isogeometric NURBS discretization.

The flow in the diffuser was initialized with zero velocity everywhere in the domain except at the inflow boundary, where the velocity profile from the channel outflow was imposed. The channel and the diffuser computations were advanced in a synchronous fashion at a time step of 0.025 based on the mean inflow velocity of unity. Meshes that are matched at the channel outflow and the diffuser inflow boundaries were employed. This allowed us to directly assign the velocity data collected from the channel outflow as inflow velocity boundary condition for the diffuser at every time step. Once the flow in the diffuser reached statistical equilibrium, velocity data was collected for over 20,000 time steps. Ensemble averaging of the data was performed by sampling the solution fields at mesh knots every 200 time steps and averaging in the span-wise direction as well as in time. We present profiles of mean stream-wise velocity at four different locations in the stream-wise direction, viz. $x = 6.4, x = 22.4, x = 38.4, x = 58.4$ (see Fig. 5).

We compare our results with the simulation of Wu et al. [52] as well as with experiments of Obi et al. [41]. The motivation of comparing with Wu stems from the fact that it is the finest resolution available for an identical problem setup (i.e., for the same problem geometry, material data and boundary conditions). Wu employed a finite volume method with a resolution of 590 cells in the x-, 100 cells in the y-, and 110 cells in the z-direction. Fig. 5 shows the mean stream-wise velocity profiles. The overall agreement in the mean stream-wise velocity profiles between our computations

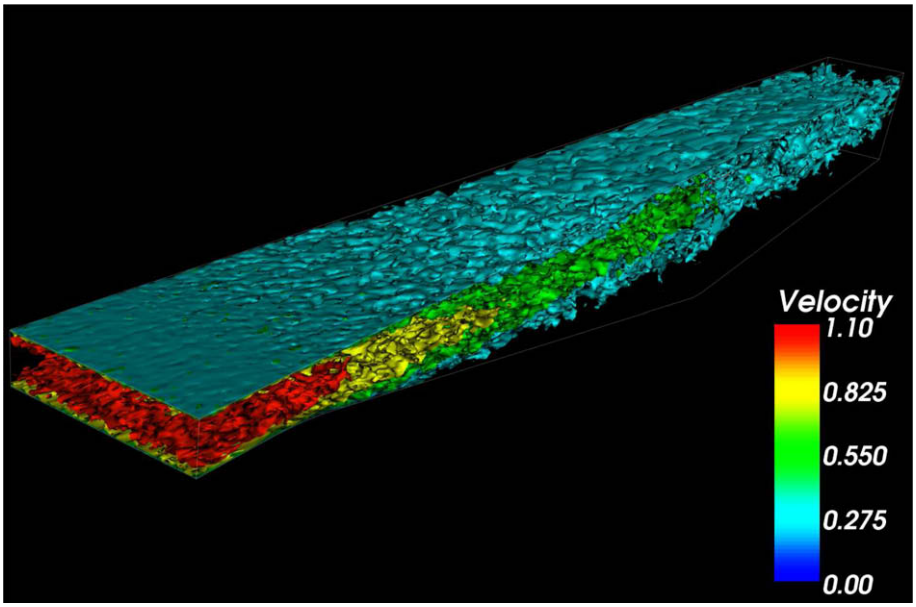

Fig. 6. Asymmetric diffuser problem. Isosurfaces of the velocity magnitude.

and the reference results is very good. We obtain an excellent match at $x = 6.4$ with both experimental and numerical reference data. At $x = 22.4$ and $x = 38.4$, the agreement with Wu's results is very good, while there is some minor deviation from the experimental data of Obi. At $x = 58.4$, near the upper wall of the diffuser our results are closer to the experimental data than to those of Wu, whereas near the lower wall and in the middle of the diffuser our results are in better agreement with the numerical reference. Point $x = 22.4$ corresponds to the onset of separation, while point $x = 58.4$ is in the reattachment region. Both separation and reattachment are well captured in our computations.

We note that the inflow channel and diffuser meshes in [17] were of similar size to the ones presented here in terms of the number of degrees of freedom. The mean and fluctuating velocity results for the inflow channel reported herein are significantly more accurate than those in [17]. Nevertheless, very good accuracy of the diffuser mean flow was attained for the best performer among several methods studied in [17], namely, CMS-PM.

Various complex features of the flow in the diffuser are presented in Figs. 6–9, where we plot the solution at an instant in time. In particular, Fig. 6 shows the isosurfaces of the fluid velocity magnitude. It is apparent from the figure that fine-grained turbulent structures are present everywhere in the diffuser. Fig. 7 shows flow velocity streamlines superposed on the pressure contours. A strong adverse pressure gradient throughout the domain with pressure fluctuations at the inflow is apparent. Moreover, the form of the streamlines suggests the presence of an internal layer as well as a clearly pronounced flow recirculation zone. Both features are also apparent in Fig. 8 which shows velocity vectors on a two-dimensional cross-section at a fixed span-wise location. Fig. 9 focuses on the recirculation zone. Note the presence of the complex vortical structures as well as the sharp internal layer. Also note the orientation and magnitude of the velocity vectors at the lower wall

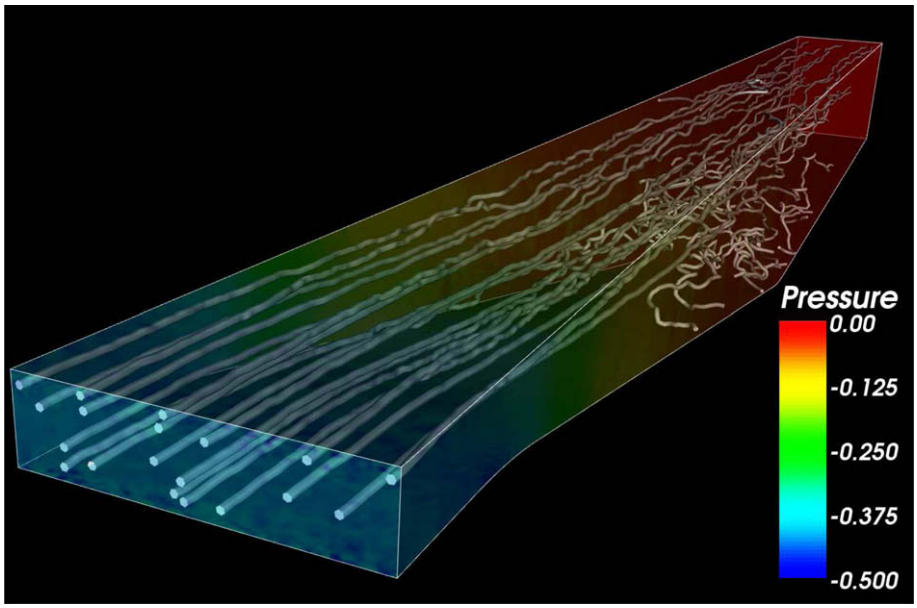

Fig. 7. Asymmetric diffuser problem. Flow velocity streamlines superposed on the pressure contours. Note the presence of a strong adverse pressure gradient.

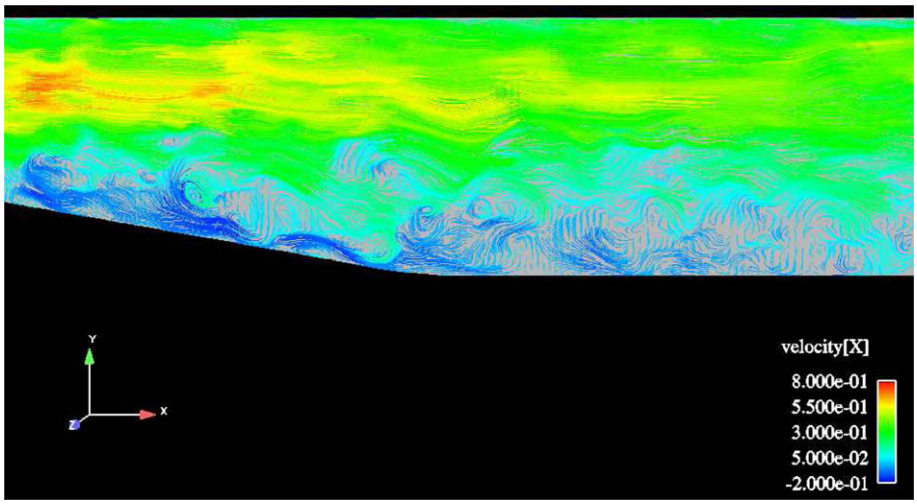

Fig. 8. Asymmetric diffuser problem. Velocity vectors colored by the value of the stream-wise velocity in the expansion channel. Detail of the region of flow separation and reattachment.

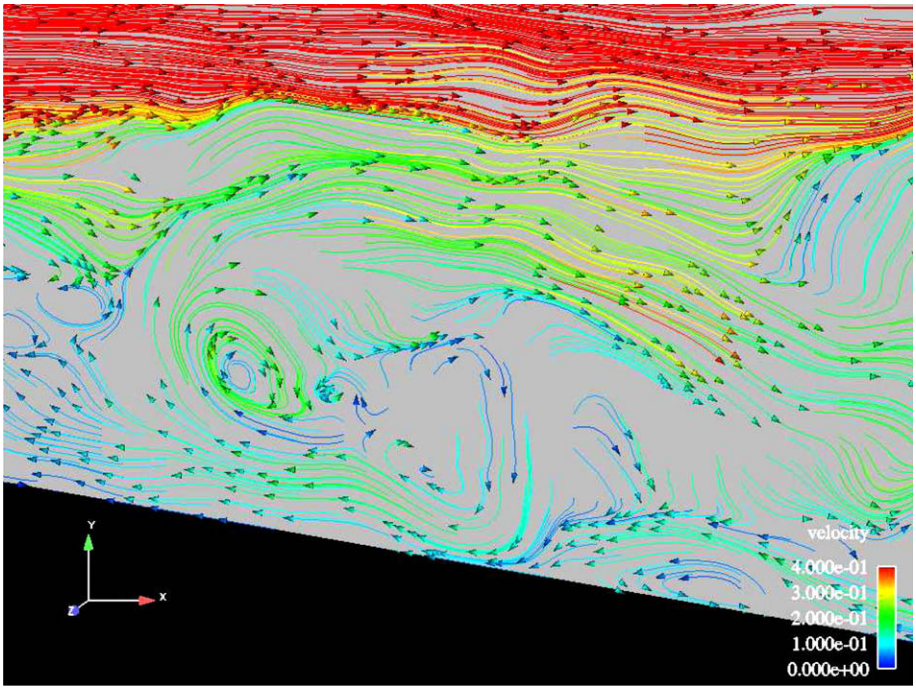

Fig. 9. Asymmetric diffuser problem. Velocity vectors colored by the magnitude of the stream-wise velocity in the expansion channel. Detail of the near-wall structures. Although all velocity components are imposed weakly, the magnitude of the wall-normal velocity is negligible in comparison to the tangential velocity at the wall.

of the diffuser. Although we impose all three velocity components weakly, the tangential velocity is significantly larger than the normal velocity. This is due to the presence of the continuity test function q^h in the weighting of the normal component of the Dirichlet condition in Eq. (9); see also Remark 3 in Section 2.

6. Conclusions

In this work, we combine three new technologies for the accurate, robust and efficient computation of incompressible wall-bounded turbulent flows, viz. NURBS-based isogeometric analysis, the residual-based variational multiscale methodology, and weak enforcement of Dirichlet boundary conditions. We further improve on the methodology proposed in previous works on this subject: Firstly, we extend the weak enforcement of Dirichlet boundary conditions to all three velocity components, which unifies the treatment of Dirichlet boundary conditions and proves to be convenient from the implementational point of view. Secondly, we introduce the assembled element-by-element inverse preconditioner for the iterative solution of the linear systems arising in the linearization of the nonlinear incompressible Navier–Stokes equations. Despite its simplicity, this preconditioner gives satisfactory iterative performance for the class of problems considered in this work. A detailed investigation of this preconditioning strategy warrants future research. Thirdly, we have devised a simple modification to a "do-nothing" outflow boundary condition which restores stability in the presence of local flow reversal at the outflow boundary. We tested this methodology on two challenging test cases, namely, turbulent channel flow at friction-velocity based Reynolds number of 2003 and turbulent flow in a planar asymmetric diffuser. We focused on the mean flow, as in RANS-type applications. The computational results obtained on relatively coarse meshes compare favorably with reference experimental and numerical data. The good agreement suggests that the proposed methodology may be well-suited for computing flows of industrial scale and relevance. We view it as an intermediate technology, somewhere between LES and RANS. It is more fundamental than RANS in that it avoids the use of ad hoc eddy viscosity models, and it can be used with coarser boundary layer grids than LES. In that regard the present approach is somewhat similar to Detached Eddy Simulations (DES) (see Spalart et al. [47]) which combines RANS modeling in the boundary layer with LES elsewhere. However, LES, DES, and the present approach are statistical approaches in the sense that the solutions need to be space and time averaged in order to obtain mean quantities. In RANS, steady state solutions are usually directly obtained, and these, by definition, correspond to mean quantities. On the other hand, as the mesh is systematically refined, the present method should converge to DNS solutions, unlike RANS.

Secondary statistics were not central to the message of this article. In order to obtain accurate secondary statistics, finer meshes than used herein are required. We hope to report on computations using the present methodology and finer meshes for problems of interest in the future.

Acknowledgement

This research was partially supported by Office of Naval Research Contract N00014-03-0263, Dr. Luise Couchman, contract monitor, and Sandia National Laboratories under contract number 114166. Y. Bazilevs and C. Michler were partially supported by the J.T. Oden ICES Postdoctoral Fellowship at the Institute for Computational Engineering and Sciences (ICES), and C. Michler was also supported through a stipend from the Netherlands Organization for Scientific Research (NWO). This support is gratefully acknowledged. The authors would also like to thank the Texas Advanced Computing Center (TACC) [49] for providing the computational resources and Greg Johnson of TACC for his assistance with flow visualization. Support of Teragrid Grant No. MCAD7S032 is gratefully acknowledged.

References

[1] I. Akkerman, Y. Bazilevs, V.M. Calo, T.J.R. Hughes, S. Hulshoff, The role of continuity in residual-based variational multiscale modeling of turbulence, Comput. Mech. 41 (2008) 371–378.

[2] D.N. Arnold, F. Brezzi, B. Cockburn, L.D. Marini, Unified analysis of discontinuous Galerkin methods for elliptic problems, SIAM J. Numer. Anal. 39 (2002) 1749–1779.

[3] Y. Bazilevs, Isogeometric Analysis of Turbulence and Fluid–Structure Interaction, Ph.D. thesis, ICES, UT Austin, 2006.

[4] Y. Bazilevs, V.M. Calo, Y. Zhang, T.J.R. Hughes, Isogeometric fluid–structure interaction analysis with applications to arterial blood flow, Comput. Mech. 38 (2006) 310–322.

[5] Y. Bazilevs, V.M. Calo, J.A. Cottrell, T.J.R. Hughes, A. Reali, G. Scovazzi, Variational multiscale residual-based turbulence modeling for large eddy simulation of incompressible flows, Comput. Methods Appl. Mech. Engrg. 197 (2007) 173–201.

[6] Y. Bazilevs, L. Beirao da Veiga, J.A. Cottrell, T.J.R. Hughes, G. Sangalli, Isogeometric analysis: approximation, stability and error estimates for *h*-refined meshes, Math. Models Methods Appl. Sci. 16 (2006) 1031–1090.

[7] Y. Bazilevs, T.J.R. Hughes, Weak imposition of Dirichlet boundary conditions in fluid mechanics, Comput. Fluids 36 (2007) 12–26.

[8] Y. Bazilevs, C. Michler, V.M. Calo, T.J.R. Hughes, Weak Dirichlet boundary conditions for wall-bounded turbulent flows, Comput. Methods Appl. Mech. Engrg. 196 (2007) 4853–4862.

[9] A.N. Brooks, T.J.R. Hughes, Streamline upwind/Petrov–Galerkin formulations for convection dominated flows with particular emphasis on the incompressible Navier–Stokes equations, Comput. Methods Appl. Mech. Engrg. 32 (1982) 199–259.

[10] C.U. Buice, J.K. Eaton, Experimental Investigation of Flow Through an Asymmetric Plane Diffuser, Thermosciences Division Report 107 Department of Mechanical Engineering, Stanford University, 1997.

[11] V.M. Calo, Residual-based Multiscale Turbulence Modeling: Finite Volume Simulation of Bypass Transistion, PhD thesis, Department of Civil and Environmental Engineering, Stanford University, 2004.

[12] J. Chung, G.M. Hulbert, A time integration algorithm for structural dynamics with improved numerical dissipation: The generalized-α method, J. Appl. Mech. 60 (1993) 371–375.

[13] R. Codina, On stabilized finite element methods for linear systems of convection–diffusion–reaction equations, Comput. Methods Appl. Mech. Engrg. 188 (2000) 61–82.

[14] J.A. Cottrell, A. Reali, Y. Bazilevs, T.J.R. Hughes, Isogeometric analysis of structural vibrations, Comput. Methods Appl. Mech. Engrg. 195 (2006) 5257–5297.

[15] R.M. Ferencz, T.J.R. Hughes, Iterative finite element solutions in nonlinear solid mechanics, in: P.G. Ciarlet, J.L. Lions (Eds.), Numerical Methods for Solids, Handbook of Numerical Analysis, vol. 6, North-Holland, 1998, pp. 3–178.

[16] V. Gravemeier, The variational multiscale method for laminar and turbulent flow, Arch. Comput. Methods Engrg. – State Art Rev. 13 (2006) 249–324.

[17] V. Gravemeier, Variational multiscale large eddy simulation of turbulent flow in a diffuser, Comput. Mech. 39 (2007) 477–495.

[18] P.M. Gresho, R.L. Sani, Incompressible Flow and the Finite Element Method, Wiley, New York, NY, 1998.

[19] J. Holmen, T.J.R. Hughes, A.A. Oberai, G.N. Wells, Sensitivity of the scale partition for variational multiscale LES of channel flow, Phys. Fluids 16 (3) (2004) 824–827.

[20] S. Hoyas, J. Jiménez, Scaling of the velocity fluctuations in turbulent channels up to $Re_\tau = 2003$, Phys. Fluids 18 (2006), doi:10.1063/1.2162185.

[21] T.J.R. Hughes, The Finite Element Method: Linear Static and Dynamic Finite Element Analysis, Dover Publications, Mineola, NY, 2000.

[22] T.J.R. Hughes, V.M. Calo, G. Scovazzi, Variational and multiscale methods in turbulence, in: W. Gutkowski, T.A. Kowalewski (Eds.), Proceedings of the XXI International Congress of Theoretical and Applied Mechanics (IUTAM), Kluwer, 2004.

[23] T.J.R. Hughes, J.A. Cottrell, Y. Bazilevs, Isogeometric analysis: CAD, finite elements, NURBS, exact geometry, and mesh refinement, Comput. Methods Appl. Mech. Engrg. 194 (2005) 4135–4195.

[24] T.J.R. Hughes, M. Mallet, A new finite element formulation for fluid dynamics: III. The generalized streamline operator for multidimensional advective–diffusive systems, Comput. Methods Appl. Mech. Engrg. 58 (1986) 305–328.

[25] T.J.R. Hughes, L. Mazzei, K.E. Jansen, Large-eddy simulation and the variational multiscale method, Comput. Visual. Sci. 3 (2000) 47–59.

[26] T.J.R. Hughes, L. Mazzei, A.A. Oberai, A.A. Wray, The multiscale formulation of large eddy simulation: decay of homogenous isotropic turbulence, Phys. Fluids 13 (2) (2001) 505–512.

[27] T.J.R. Hughes, A.A. Oberai, L. Mazzei, Large-eddy simulation of turbulent channel flows by the variational multiscale method, Phys. Fluids 13 (6) (2001) 1784–1799.

[28] T.J.R. Hughes, G. Scovazzi, L.P. Franca, Multiscale and stabilized methods, in: E. Stein, R. de Borst, T.J.R. Hughes (Eds.), Encyclopedia of Computational Mechanics, Computational Fluid Dynamics, vol. 3, Wiley, 2004 (Chapter 2).

[29] T.J.R. Hughes, G.N. Wells, A.A. Wray, Energy transfers and spectral eddy viscosity of homogeneous isotropic turbulence: comparison of dynamic Smagorinsky and multiscale models over a range of discretizations, Phys. Fluids 16 (2004) 4044–4052.

[30] K.E. Jansen, C.H. Whiting, G.M. Hulbert, A generalized-α method for integrating the filtered Navier–Stokes equations with a stabilized finite element method, Comput. Methods Appl. Mech. Engrg. 190 (1999) 305–319.

[31] K.E. Jansen and A.E. Tejada-Martinez, An evaluation of the variational multiscale model for large-eddy simulation while using a hierarchical basis, in: AIAA Paper 2002-0283, 2002.

[32] H.-J. Kaltenbach, M. Fatica, R. Mittal, T.S. Lund, P. Moin, Study of flow in a planar asymmetric diffuser using large-eddy simulation, J. Fluid Mech. 390 (1999) 151–185.

[33] B. Koobus, C. Farhat, A variational multiscale method for the large eddy simulation of compressible turbulent flows on unstructured meshes – application to vortex shedding, Comput. Methods Appl. Mech. Engrg. 193 (2004) 1367–1383.

[34] A.G. Kravchenko, P. Moin, R. Moser, Zonal embedded grids for numerical simulation of wall-bounded turbulent flows, J. Comput. Phys. 127 (1996) 412–423.

[35] A.G. Kravchenko, P. Moin, K. Shariff, B-spline method and zonal grids for simulation of complex turbulent flows, J. Comput. Phys. 151 (1999) 757–789.

[36] W.Y. Kwok, R.D. Moser, J. Jiménez, A critical evaluation of the resolution properties of B-spline and compact finite difference methods, J. Comput. Phys. 174 (2001) 510–551.

[37] Linear Algebra Package (LAPACK). <http://www.netlib.org/lapack/>.

[38] M. Manguoglu, A.H. Sameh, T.E. Tezduyar, S. Sathe, A nested iterative scheme for computation of incompressible flows in long domains, Comput. Mech. (2008), doi:10.1007/s00466-008-0276-0. Published online.

[39] R. Moser, J. Kim, R. Mansour, DNS of turbulent channel flow up to Re = 590. Physics of Fluids 11 (1999) 943–945.

[40] A.A. Oberai and T.J.R. Hughes, The variational multiscale formulation of LES: channel flow at $Re_\tau = 590$, 40th AIAA Ann. Mtg., Reno, NV, 2002. AIAA 2002-1056.

[41] S. Obi, K. Aoki, and S. Masuda Experimental and computational study of turbulent separating flow in an asymmetric plane diffuser, Ninth symposium on turbulent shear flows, Kyoto, Japan, August 16-19, 1993.

[42] S. Ramakrishnan, S.S. Collis, Partition selection in multiscale turbulence modeling, Phys. Fluids 18 (7) (2006).

[43] Y. Saad, Iterative Methods for Sparse Linear Systems, Second ed., SIAM, Philadelphia, 2003.

[44] Y. Saad, M.H. Schultz, GMRES: a generalized minimal residual algorithm for solving nonsymmetric linear systems, SIAM J. Sci. Statist. Comput. 7 (1986) 856–869.

[45] F. Shakib, T.J.R. Hughes, Z. Johan, A new finite element formulation for computational fluid dynamics: X. The compressible Euler and Navier–Stokes equations, Comput. Methods Appl. Mech. Engrg. 89 (1991) 141–219.

[46] K. Shariff, R.D. Moser, Two-dimensional mesh embedding for B-spline methods, J. Comput. Phys. 145 (1998) 471–488.

[47] P.R. Spalart, W.H. Jou, M. Stretlets, S.R. Allmaras, Comments on the Feasibility of LES for Wings and on a Hybrid RANS/LES Approach, Advances in DNS/LES, Greyden Press, Columbus, 1997.

[48] D.B. Spalding, A single formula for the law of the wall, J. Appl. Mech. 28 (1961) 444–458.

[49] Texas Advanced Computing Center (TACC). <http://www.tacc.utexas.edu>.

[50] T.E. Tezduyar, Computation of moving boundaries and interfaces and stabilization parameters, Int. J. Numer. Methods Fluids 43 (2003) 555–575.

[51] M.F. Wheeler, An elliptic collocation-finite element method with interior penalties, SIAM J. Numer. Anal. 15 (1978) 152–161.

[52] X. Wu, J. Schlutter, P. Moin, H. Pitsch, G. Iaccarino, F. Ham, Computational study on the internal layer in a diffuser, J. Fluid Mech. 550 (2006) 391–412.

[53] Y. Zhang, Y. Bazilevs, S. Goswami, C. Bajaj, T.J.R. Hughes, Patient-specific vascular NURBS modeling for isogeometric analysis of blood flow, Comput. Methods Appl. Mech. Engrg. 196 (2007) 2943–2959.